Supplementary Information of

Persistent Fermi Pockets and Robust Electron Pairing in Lightly Doped CuO_2 Planes of Cuprate Superconductors

Hao Chen[1,2,†], Jumin Shi[1,2,†], Yinghao Li[1,2,†], Xiangyu Luo[1,†], Yiwen Chen[1,2], Chaohui Yin[1], Yingjie Shu[1,2], Jiuxiang Zhang[1], Taimin Miao[1,2], Bo Liang[1,2], Wenpei Zhu[1,2], Neng Cai[1,2], Xiaolin Ren[1,2], Chengtian Lin[3], Shenjin Zhang[4], Zhimin Wang[4], Fengfeng Zhang[4], Feng Yang[4], Qinjun Peng[4], Zuyan Xu[4], Guodong Liu[1,2,5], Hanqing Mao[1,2,5], Xintong Li[1,2,5], Tao Xiang[1,2,5,6], Lin Zhao[1,2,5,*] and X. J. Zhou[1,2,5,*]

[1]*Beijing National Laboratory for Condensed Matter Physics, Institute of Physics, Chinese Academy of Sciences, Beijing 100190, China.*

[2]*University of Chinese Academy of Sciences, Beijing 100049, China.*

[3]*Max Planck Institute for Solid State Research, Heisenbergstrasse 1, D-70569 Stuttgart, Germany.*

[4]*Technical Institute of Physics and Chemistry, Chinese Academy of Sciences, Beijing 100190, China.*

[5]*Songshan Lake Materials Laboratory, Dongguan, Guangdong 523808, China.*

[6]*Beijing Academy of Quantum Information Sciences, Beijing 100193, China.*

[†]*These authors contributed equally to this work.*

[*]*Corresponding author: LZhao@iphy.ac.cn, XJZhou@iphy.ac.cn*

(Dated: May 10, 2026)

1. Real-space mapping and Fermi surface analysis of different regions on the UD95K-Bi2223 sample surface.

Supplementary Figure 1 presents real-space mappings and Fermi surface analyses of various regions on the UD95K-Bi2223 sample surface. In Supplementary Fig. 1a, the entire sample surface is scanned, and the Fermi surface is measured at each spatial location. Three representative regions, outlined in yellow rectangles, are shown in expanded views in Supplementary Fig. 1b–d. Four selected spots, highlighted by blue rectangles, exhibit Fermi surfaces shown in Supplementary Fig. 1e–h, corresponding to regions with one, two, and three Fermi surface sheets, respectively. Specifically, Supplementary Fig. 1e shows a single sheet, Supplementary Fig. 1f shows two sheets, and Supplementary Fig. 1g,h show three sheets. Supplementary Fig. 1i–l display high-statistics Fermi surface mappings of the same four spots shown in Supplementary Fig. 1e–h.

2. Momentum-dependent band structures measured in region 2 (5-layer) of the UD30K-Bi2223 sample at 15 K and photoemission spectra and energy gaps along the IP_1 Fermi pocket.

Supplementary Figure 3a shows band structures along seven momentum cuts in region 2 (5-layer) of the UD30K-Bi2223 sample, extending from the nodal direction (Cut 1) to the (π,0)–(0,π) direction (Cut 7) around the $(\pi/2, \pi/2)$ point. The positions of these cuts are indicated by black lines in Supplementary Fig. 3c. For clarity, the corresponding second-derivative EDC images are presented in Supplementary Fig. 3b, with the observed IP_1 bands marked by red arrows in both panels. Supplementary Fig. 3d displays EDCs along the IP_1 Fermi pocket, with Fermi momenta represented by the angle θ, as defined in the inset of Supplementary Fig. 3f. Symmetrized EDCs derived from these spectra are shown in Supplementary Fig. 3e, and the momentum-dependent energy gaps, extracted from the symmetrized EDCs, are plotted versus θ in Supplementary Fig. 3f.

3. Simulations of Fermi pockets and band structures in multilayer cuprates.

The formation of Fermi pockets is effectively captured by the mean-field t–U model[1–5]. For a single CuO_2 plane at half filling, the two-dimensional Hubbard Hamiltonian reads[1, 2, 5]

$$H = -t \sum_{\langle ij \rangle \sigma} c^{\dagger}_{i\sigma} c_{j\sigma} - t' \sum_{\langle\langle ij \rangle\rangle \sigma} c^{\dagger}_{i\sigma} c_{j\sigma} - t'' \sum_{\langle\langle\langle ij \rangle\rangle\rangle \sigma} c^{\dagger}_{i\sigma} c_{j\sigma} + U \sum_{i} n_{i\uparrow} n_{i\downarrow} - \mu \sum_{i\sigma} n_{i\sigma} \tag{1}$$

where t, t' and t'' denote nearest-, second-nearest- and third-nearest-neighbor hoppings, respectively, and U represents the on-site Coulomb repulsion. Fourier transforming to momentum space yields

$$H = \sum_{k\sigma} \varepsilon_k c^{\dagger}_{k\sigma} c_{k\sigma} + \frac{U}{2} \sum_{k_i \sigma_i} c^{\dagger}_{k_1\sigma_1} c^{\dagger}_{k_2\sigma_2} c_{k_3\sigma_3} c_{k_4\sigma_4} \delta_{\sigma_1\sigma_4} \delta_{\sigma_2\sigma_3} \tag{2}$$

where ε_k represents the bare dispersion of the single CuO_2 plane. It is well known that at half filling, the 2D Hubbard model has an antiferromagnetic ground state. At large U, in the mean-field (MF) approach[2], Eq. 2 takes the form

$$H_{\mathrm{MF}} = {\sum_{k\sigma}}' \left(\varepsilon_k c^{\dagger}_{k\sigma} c_{k\sigma} + \varepsilon_{k+Q} c^{\dagger}_{k+Q,\sigma} c_{k+Q,\sigma} \right) - \Delta_{MF} {\sum_{k\sigma}}' \left(c^{\dagger}_{k\sigma} c_{k+Q,\sigma} + c^{\dagger}_{k+Q,\sigma} c_{k\sigma} \right) \tag{3}$$

where Δ_{MF} is the mean-field gap and $Q = (\pi, \pi)$ is the antiferromagnetic wave vector. The Hamiltonian can also be expressed as

$$H = \psi^{\dagger} \begin{pmatrix} \varepsilon_k & \Delta_{MF} \\ \Delta_{MF} & \varepsilon_{k+Q} \end{pmatrix} \psi \quad , \quad \psi = \begin{pmatrix} c_k \\ c_{k+Q} \end{pmatrix} \tag{4}$$

The bare dispersion ε_k is described by the tight binding model:

$$\varepsilon_k = -2t[cos(k_x a) + cos(k_y a)] - 4t' cos(k_x a) cos(k_y a) - 2t''[cos(2k_x a) + cos(2k_y a)] - \mu \tag{5}$$

and

$$\begin{aligned} \varepsilon_{k+Q} =& -2t[cos((k_x a + \pi)) + cos((k_y a + \pi))] - 4t' cos((k_x a + \pi)) cos((k_y a + \pi)) \\ & - 2t''[cos(2(k_x a + \pi)) + cos(2(k_y a + \pi))] - \mu \end{aligned} \tag{6}$$

The observed IP_0 and IP_1 Fermi pockets and momentum-dependent band structures are fitted based on the Hamiltonian (Eq. 4). The fitted parameters are shown in Fig. 4f.

ARPES measures the single particle spectral function $A(k, \omega)$:

$$I_{ARPES} = I_0 \cdot A(k, \omega) \cdot f(\omega, T) \tag{7}$$

where I_0 is a prefactor and $f(\omega, T)$ is the Fermi-Dirac distribution function. The single particle spectral function $A(k, \omega)$ is the imaginary part of the Green's function $G(k, \omega)$

$$A(k, \omega) = -\frac{1}{\pi} Im[G(k, \omega)] \tag{8}$$

The Green's function is obtained from the Hamiltonian:

$$G(k, \omega) = (\omega - \Sigma(k, \omega) - H)^{-1} \tag{9}$$

where $\Sigma(k, \omega)$ is the electron self-energy.

$$\Sigma(k, \omega) = \Sigma'(k, \omega) + i\Sigma''(k, \omega) \tag{10}$$

$\Sigma'(k, \omega)$ and $\Sigma''(k, \omega)$ are the real part and imaginary part of $\Sigma(k, \omega)$, respectively. We simulate the spectrum with self-energy of the marginal Fermi liquid to describe the interaction between the electrons.

$$\Sigma''(k, \omega) = \lambda\sqrt{\omega^2 + (\pi k_B T)^2} + \Gamma_0 \tag{11}$$

We ignor the real part of the self-energy and use the tight binding model in Eq. 5 to describe the band dispersion.

The IP_0 and IP_1 Fermi pockets and their band structures are simulated using the fitted parameters. Supplementary Fig. 4 shows a simulated Fermi pocket and band structures and their comparison with the measured ones. Supplementary Fig. 5 shows the spectral weight distribution along the simulated Fermi pocket which is the same as the one shown in Supplementary Fig. 4. They indicate that the simulated results are in good agreement with the experimental ones.

Supplementary Table 1. **Summary of the IP_0 and IP_1 Fermi pockets observed in different regions of various Bi2223 samples.**

Bi2223 Sample	**Sample Region**	**Number of Fermi Surface Sheets**	**Number of CuO_2 Planes, n**	**Pocket Name**	**Doping Level (%)**	**Major Axis Length u (π/a)**	**Minor Axis Length u (π/a)**	**u/v**	**Maxmium Gap Δ_{max} (meV)**
UD30K	UD30K-R1	3	5	UD30K-R1-L5-IP0	1.97	0.10	0.06	1.84	0
	UD30K-R2	3	5	UD30K-R2-L5-IP0	0.74	0.07	0.04	1.82	0
				UD30K-R2-L5-IP1	2.00	0.11	0.06	1.83	12
UD95K	UD95K-R1	3	6	UD95K-R1-L6-IP0	1.03	0.07	0.04	1.62	0
				UD95K-R1-L6-IP1	5.12	0.18	0.09	2.01	12
	UD95K-R2	3	5	UD95K-R2-L5-IP0	2.28	0.12	0.06	1.90	0
				UD95K-R2-L5-IP1	5.52	0.19	0.09	2.09	13
OP111K	OP111K-R1	4	8	OP111K-R1-L8-IP0	1.73	0.10	0.06	1.72	0
				OP111K-R1-L8-IP1	6.34	0.20	0.10	1.89	30
	OP111K-R2	3	6	OP111K-R2-L6-IP0	2.56	0.12	0.07	1.68	0
				OP111K-R2-L6-IP1	8.78	0.23	0.12	1.92	33
	OP111K-R3	4	7	OP111K-R3-L7-IP0	3.45	0.15	0.07	2.05	0
				OP111K-R3-L7-IP1	6.83	0.21	0.10	2.00	21
	OP111K-R4	5	5	OP111K-R4-L5-IP0	3.70	0.15	0.08	1.99	0
				OP111K-R4-L5-IP1	7.43	0.22	0.11	1.98	33

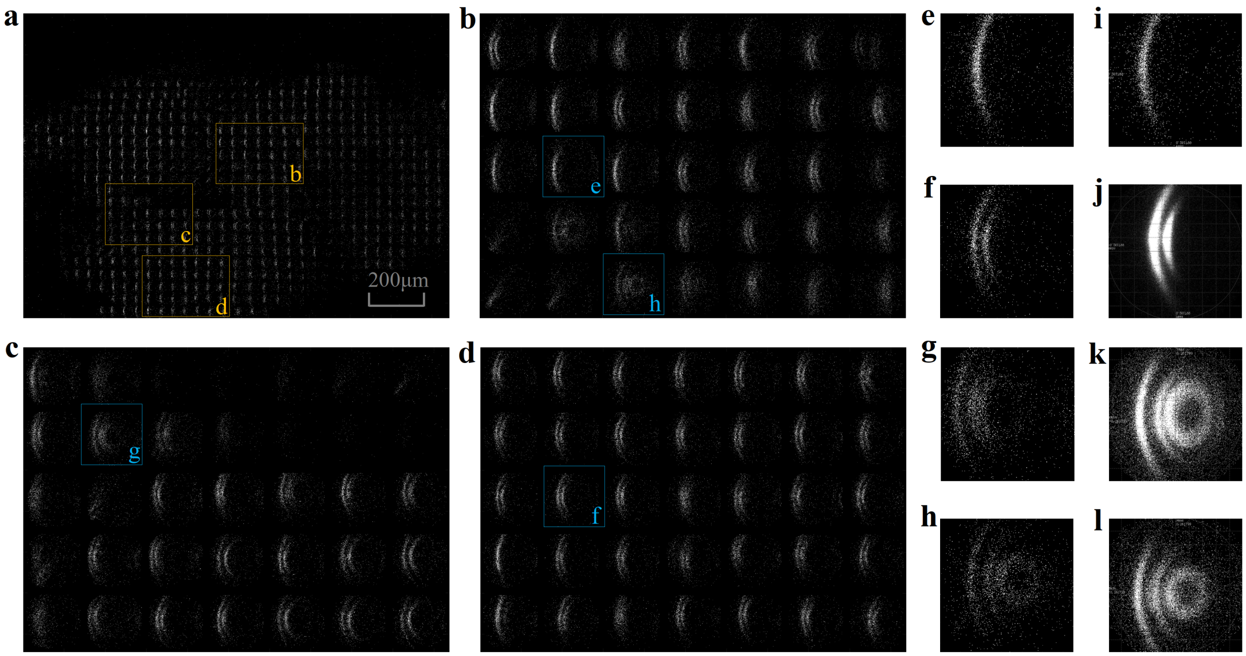

Supplementary Fig. 1. **Real-space mapping and Fermi surface analysis of various regions on the UD95K-Bi2223 sample surface. a**, Real-space scan of the entire sample surface with the Fermi surface measured at each location. **b-d**, Expanded views of the three regions outlined by yellow rectangles in **a**. **e**, Fermi surface at the spot highlighted by a blue rectangle in **b**, showing a single sheet. **f**, Fermi surface at the spot highlighted by a blue rectangle in **d**, showing two sheets. **g**, Fermi surface at the spot highlighted by a blue rectangle in **c**, showing three sheets. **h**, Fermi surface at the spot highlighted by a blue rectangle in **b**, also showing three sheets. **i-l**, Highstatistics Fermi surface mappings corresponding to **e–h**.

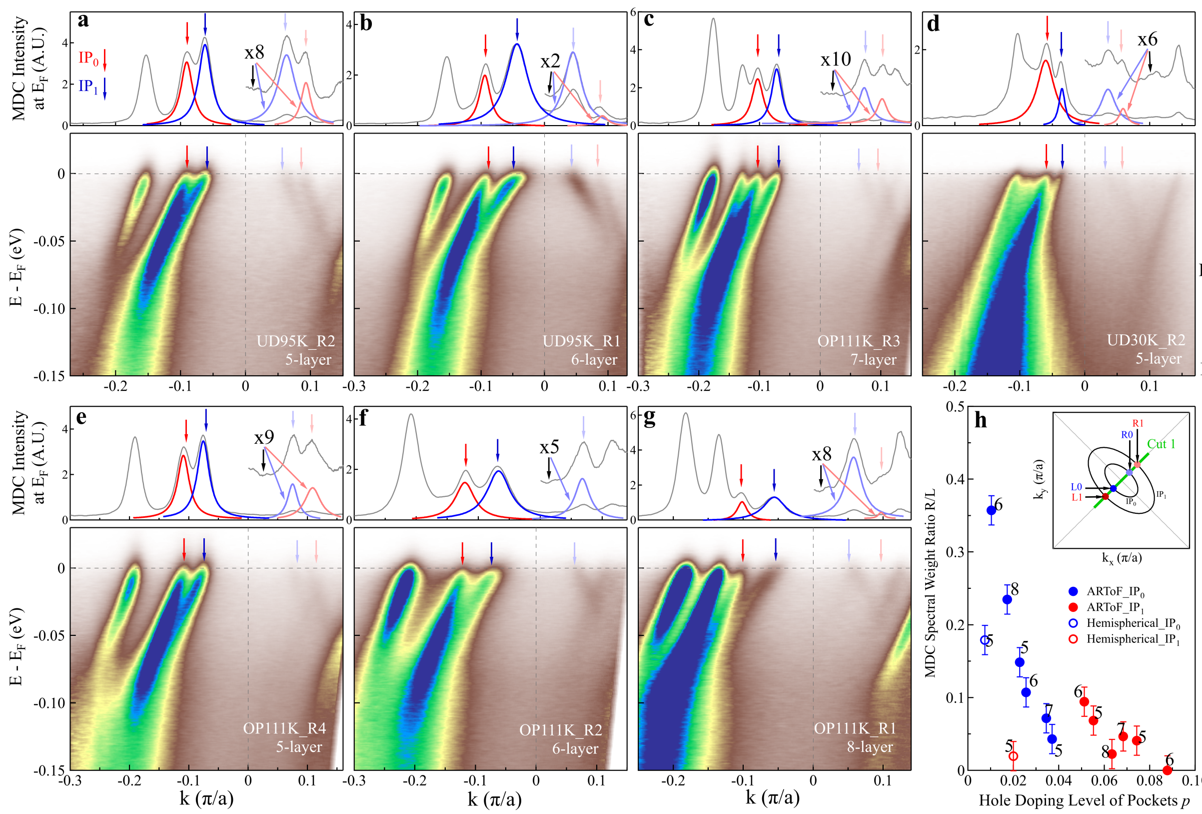

Supplementary Fig. 2. **Nodal band structures and spectral weight distribution for the measured Fermi pockets. a-g**, Band structures measured along the nodal cut (lower panels) and the corresponding MDCs at the Fermi level (upper panels). The location of the momentum cut is shown in the inset of **h** as a green line. The observed IP_0 and IP_1 bands are marked by blue and red arrows, respectively. The corresponding MDC peaks are fitted by Lorentzians and each peak area of the IP_0 and IP_1 bands can be obtained. To see the weak signal on the right side more clearly, the right side of the MDCs and the corresponding fitted Lorentzians are rescaled by a factor. **h**, Ratio of right-to-left MDC spectral weights for various doping levels. Along the nodal direction (zero gap), left (L0/L1) and right (R0/R1) vertices of the IP_0/IP_1 pockets are compared; blue and red circles denote R0/L0 and R1/L1 ratios, respectively. Layer numbers for each data point are indicated. The error bars reflect the uncertainty in determining the spectral weight.

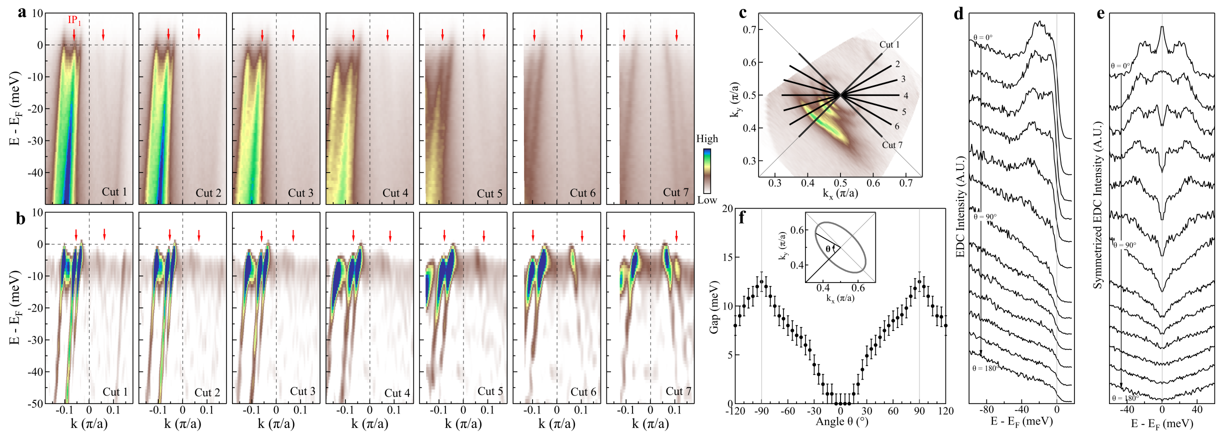

Supplementary Fig. 3. **Band structures of Fermi pockets measured in region 2 (5-layer) of the UD30K-Bi2223 sample at 15 K and momentum-dependent photoemission spectra and energy gaps along the IP_1 Fermi pocket. a**, Band structures measured along different momentum cuts. The location of the momentum cuts is shown in **c** as black lines. The observed IP_1 bands are marked by red arrows. **b**, Corresponding EDC second-derivative images from **a**. **c**, Fermi surface mapping with the momentum cuts marked. **d**, EDCs along the IP_1 Fermi pocket. The position of the Fermi momenta is represented by the angle θ as defined in the inset of **f**. **e**, Symmetrized EDCs from **d**. **f**, Momentum-dependent energy gaps along the IP_1 Fermi pocket plotted as a function of the angle θ. The energy gaps are obtained from symmetrized EDCs in **e**. The error bars reflect the uncertainty in determining the gap size.

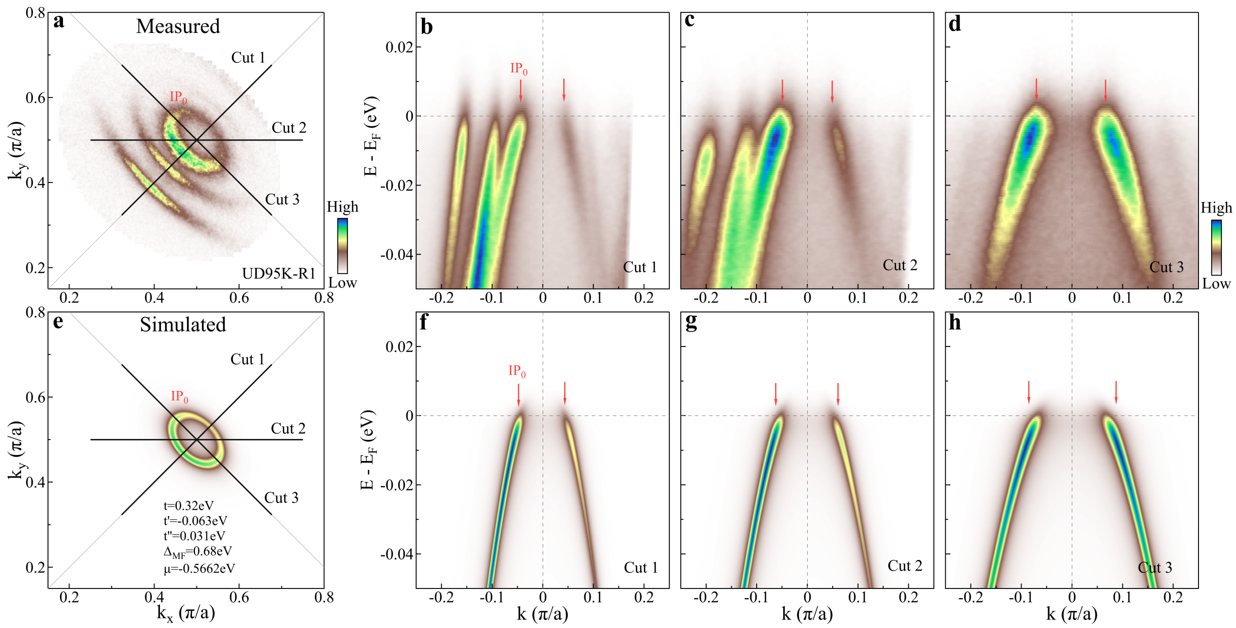

Supplementary Fig. 4. **Comparison of simulated and measured Fermi pockets and band structures.** **a**, Fermi pockets measured in region 1 (6-layer) of the UD95K-Bi2223 sample at 15 K with the IP_0 Fermi pocket marked. **b-d**, Band structures measured along different momentum cuts. The location of the momentum cuts is shown in **a** as black lines. The observed IP_0 bands are marked by red arrows. **e**, Simulated IP_0 Fermi pocket using the mean-field t–U model with $t = 0.32\,\mathrm{eV}$, $t' = -0.063\,\mathrm{eV}$, $t'' = 0.031\,\mathrm{eV}$, $\Delta_{\mathrm{MF}} = 0.68\,\mathrm{eV}$, and $\mu = -0.5662\,\mathrm{eV}$. **f-h**, Simulated IP_0 band structures along different momentum cuts. The location of the momentum cuts is shown in **e** as black lines which is the same as those in **a**.

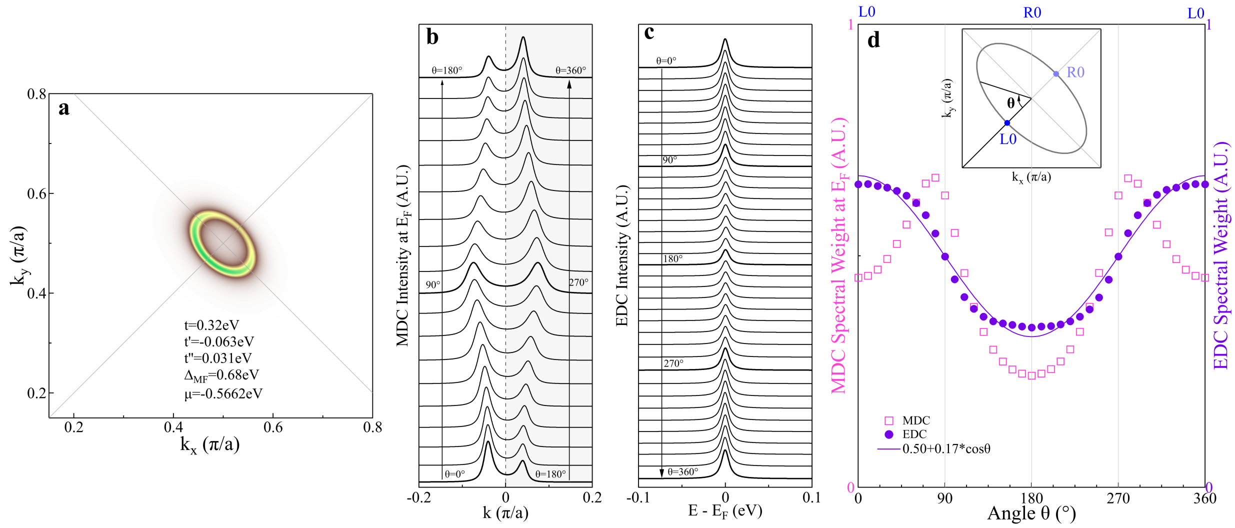

Supplementary Fig. 5. **Spectral weight distribution along the simulated Fermi pocket.** **a**, Simulated Fermi pocket by using the mean-field t-U model with t=0.32 eV, t'=-0.063 eV, t''=0.031 eV, Δ_{MF}=0.68 eV and μ=-0.5662 eV. It is the same as the one shown in Fig. S4. **b**, MDCs at the Fermi level along different momentum cuts crossing the $(\pi/2, \pi/2)$ point. The momentum cuts are represented by the angle θ which is defined in the inset of **d**. **c**, EDCs along the simulated Fermi pocket. The position of the Fermi momentum is represented by the angle θ. **d**, Spectral weight distribution along the simulated Fermi pocket. The spectral weight is obtained by two ways. One is to get MDC peak area from **b** (plotted as pink squares). The other is to get the EDC peak area from the EDCs in **c** (purple circles). The EDC spectral weight distribution basically follows the $a + b\cos\theta$ relation with a=0.50 and b=0.17 (purple line). Inset: definition of θ and labeling of minor-axis vertices L0 (0°, 360°) and R0 (180°).

Supplementary References

[1] J. R. Schrieffer, X. G. Wen, and S. C. Zhang. Dynamic spin fluctuations and the bag mechanism of high-T_c superconductivity. *Physical Review B* **39**, 11663 (1989).

[2] A. V. Chubukov and D. M. Frenkel. Renormalized perturbation theory of magnetic instabilities in the two-dimensional Hubbard model at small doping. *Physical Review B* **46**, 11884 (1992).

[3] N. Bulut, D. J. Scalapino, and S. R. White. Electronic properties of the insulating half-filled hubbard model. *Physical Review Letters* **73**, 748 (1994).

[4] T. Xiang and J. M. Wheatley. Quasiparticle energy dispersion in doped two-dimensional quantum antiferromagnets. *Physical Review B* **54**, R12653 (1996).

[5] C. Kusko, R. S. Markiewicz, M. Lindroos, and A. Bansil. Fermi surface evolution and collapse of the Mott pseudogap in $Nd_{2-x}Ce_xCuO_{4\pm\delta}$. *Physical Review B* **66**, 140513 (2002).